

MF-NeRF: Memory Efficient NeRF with Mixed-Feature Hash Table

Yongjae Lee¹, Li Yang², Deliang Fan¹

¹Johns Hopkins University

²University of North Carolina at Charlotte

ylee236@jhu.edu, lyang50@charlotte.edu, dfan10@jhu.edu

Abstract

Neural radiance field (NeRF) has shown remarkable performance in generating photo-realistic novel views. Among recent NeRF related research, the approaches that involve the utilization of explicit structures like grids to manage features achieve exceptionally fast training by reducing the complexity of multilayer perceptron (MLP) networks. However, storing features in dense grids demands a substantial amount of memory space, resulting in a notable memory bottleneck within computer system. Consequently, it leads to a significant increase in training times without prior hyper-parameter tuning. To address this issue, in this work, we are the first to propose MF-NeRF, a memory-efficient NeRF framework that employs a Mixed-Feature hash table to improve memory efficiency and reduce training time while maintaining reconstruction quality. Specifically, we first design a *mixed-feature hash encoding* to adaptively mix part of multi-level feature grids and map it to a single hash table. Following that, in order to obtain the correct index of a grid point, we further develop an *index transformation* method that transforms indices of an arbitrary level grid to those of a canonical grid. Extensive experiments benchmarking with state-of-the-art Instant-NGP, TensorRF, and DVGO, indicate our MF-NeRF could achieve the fastest training time on the same GPU hardware with similar or even higher reconstruction quality.

1 Introduction

Representing 3D scenes has garnered significant recognition in various industries. In the past, the conventional method involved breaking down free surfaces into primitive triangles, also known as polygons. However, this approach has been proven to be costly, so it often simplifies the scene to reduce the cost which in turn leads to a sacrifice in the quality of reconstruction. Recently, the developments of machine learning have brought new possibilities for scene representation (Niemeyer et al. 2020; Park et al. 2019). Notably, the neural radiance field (NeRF) (Mildenhall et al. 2020) has made a significant advancement in both the quality and efficiency of synthesizing novel views, which learns a 3D scene by training multi-layer perceptrons (MLPs).

In general, NeRF has two main research directions in encoding a 3D scene: implicit and explicit representations. In the implicit representation-based methods (Guo, Li, and Lee

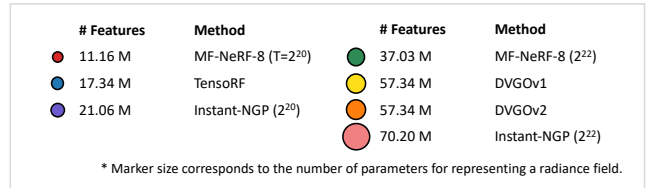
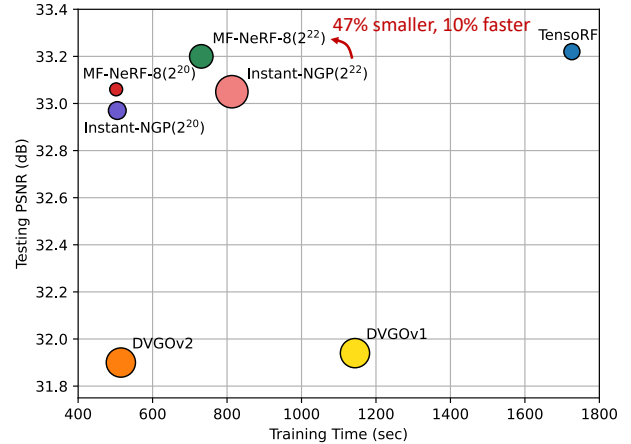


Figure 1: Comparison of training time and rendering quality on the Synthetic NeRF dataset. Our MF-NeRF efficiently represents scenes using less parameters, enhanced by sharing features across multi-resolution grids. Remarkably, it uses only half of the parameters, and less training time, as Instant-NGP with the same hash table size T .

2022; Martin-Brualla et al. 2021; Schwarz et al. 2020; Hong et al. 2022; Turki, Ramanan, and Satyanarayanan 2022; Chen et al. 2022c), it is crucial to provide inputs of sufficient size to encode high-dimensional and complex radiance fields into MLP networks. As one common approach, the positional encoding (Mildenhall et al. 2020; Vaswani et al. 2017) method decomposes low-dimensional spatial-directional inputs into a set of high-dimensional frequency parameters, helping MLP networks learn complex curves and view-dependent light effects. For processing high-dimensional inputs effectively, the structure of MLP networks needs to be both deep and wide. Additionally, due to the infinite and continuous nature of the space, a multitude of giant MLP

network queries are required to learn every direction through every point. As a result, the training time and rendering time are typically very large.

Differently, other prior works (Liu et al. 2020; Yu et al. 2021; Takikawa et al. 2021; Chen et al. 2022b; Hedman et al. 2021) address the issue of MLP complexity by abstracting and managing scenes as features through explicit representation. They mainly utilize a feature grid that can inherently represent spatial information through voxel coordinates, enabling the design of small and efficient MLPs. While these approaches drastically reduce the computing time for learning and rendering, they typically require enormous GPU memory for storing the large, dense feature grids. To address such memory bottleneck challenge, feature compression methods have been discussed (Chen et al. 2022a,a). As a representative work, Instant-NGP (Müller et al. 2022) proposes multi-resolution hash table to manage multiple grids of different resolutions and then compress them by mapping into smaller hash tables. However, having more features in the grid requires a larger allocation of memory space for the big hash tables and cache buffering in memory. If such memory space is much larger than computer cache memory, the training time will increase significantly due to greatly increased cache miss ratio, without a corresponding improvement in rendering quality, as shown in the analysis of Instant-NGP with hash table sizes ranging from 2^{20} to 2^{22} in 1. In real applications, this memory bottleneck issue can arise as a major problem when learning on large scenes, such as buildings (Tancik et al. 2022).

To address such challenge, following the explicit representation approach, we propose MF-NeRF, a memory efficient NeRF framework with a novel **Mixed-Feature (MF) hash encoding** method to reduce memory usage and training time, while preserving the quality of reconstruction. Our proposed MF hash encoding maps multiple feature grids into a shared MF hash table, enabling the learning of combined/mixed coarse and fine abstracted features among grids. As a consequence, MF-NeRF could significantly compress the conventional multiresolution hash feature encoding, leading to a great reduction in training time while maintaining high rendering quality (e.g., MF-NeRF-8 (2^{22}) outperforms Instant-NGP (2^{22}) on the same GPU with 47% smaller model size and 10% reduction in training time, in Fig. 1). Our contributions are as follows:

- We propose MF-NeRF, an efficient NeRF framework that aims to reduce parameter size and training time while keeping the reconstruction quality high. We first design a *mixed-feature hash encoding* to adaptively mix partial feature grids into a single hash table. To ensure accurate feature vector retrieval from this table, we further design an *index transformation* technique that standardizes grid indices from distinct grid spaces to a shared grid space.
- We conduct extensive experiments to benchmark MF-NeRF against state-of-the-art (SOTA) methods such as Instant-NGP, TensoRF, and DVGO. Our MF-NeRF method achieves the fastest training time on the same GPU hardware while maintaining similar or higher rendering quality. For example, compared to Instant-NGP,

our MF-NeRF-8 (2^{22}) setup achieves around 10% training time reduction on the same GPU with 0.15 higher average PSNR on the synthetic NeRF dataset.

2 Related work

2.1 Neural Scene Representations

Inspired by NeRF (Mildenhall et al. 2020), many works (Lin et al. 2021; Barron et al. 2021; Hwang, Kim, and Kim 2023; Yen-Chen et al. 2021; Suhail et al. 2022; Orsingher et al. 2022; Kurz et al. 2022; Chen et al. 2022d) have been proposed for novel view synthesis tasks. Generally, NeRF (Mildenhall et al. 2020) encodes a scene into a couple of MLP networks, using multiple posed images. Therefore, having consistency between images is crucial, as NeRF struggles to learn the scene when provided with inaccurate pose information or impaired images. Earlier works such as Deblur-NeRF (Ma et al. 2022) and PDRF (Peng and Chellappa 2022) have investigated approaches to train a clear scene from blurry images. Deblur-NeRF optimizes a separate neural network that generates rays to simulate camera motion and defocus blurs, thereby enabling NeRF to capture and represent deblurred scenes. Similarly, in cases where image noise arises from low-light environments or overheated sensors, PDRF (Mildenhall et al. 2022) approaches the problem by modeling the noise using color blending, preventing NeRF from learning it. On the other hand, NAN (Pearl, Treibitz, and Korman 2022) focuses on generating a clean image with the same view from a burst of noisy images that have relatively small camera movement, in contrast to what Deblur-NeRF and PDRF assume. In addition, Ev-NeRF (Hwang, Kim, and Kim 2023) demonstrated NeRF is trainable with event camera data rather than regular posed RGB images.

Methods that leverage scene prior information continue to be an active area of research (Lee and Lee 2023; Orsingher et al. 2022). NerfingMVS (Wei et al. 2021) trains a neural network that completes sparse point clouds generated by Structure-from-Motion (Schoenberger and Frahm 2016) into dense point clouds to help NeRF better understand the scene with the geometry. DS-NeRF (Deng et al. 2022) uses sparse point clouds to help learn the density distribution of the scene. MVG-NeRF (Orsingher et al. 2022) utilizes depth maps generated by multi-view stereo (Schönberger et al. 2016) and compares them with synthesized depth maps produced by neural rendering methods. On the other hand, iNeRF (Yen-Chen et al. 2021) propose a localization method that estimates the poses of given images by comparing them with neural-rendered images based on possible poses.

NeRF updates the entire MLP network for a given image set, which means it can learn only one scene at a time. Recent research (Wang et al. 2021, 2022; Johari, Lepoittevin, and Fleuret 2022) has proved that transformers (Vaswani et al. 2017) can be employed to select images from a given set for synthesizing novel view images, rather than directly encoding a scene into MLPs. Additionally, considering epipolar geometry constraints can enhance the restoration of view-dependent lighting effects (Suhail et al. 2022).

2.2 Efficient NeRF Rendering Algorithms

To address the slow training and long rendering time of NeRF, recent research has begun to use explicit data structures for storing and accessing features that encode the shape and color information of a scene (Liu et al. 2020; Martel et al. 2021; Hedman et al. 2021). NSVF (Liu et al. 2020) employs an Octree to store optimized scene features. This approach supports the gradual subdivision of voxels and the pruning of empty cells, which allows increased scene resolution and improved rendering quality. DVGO (Sun, Sun, and Chen 2022a) adaptively increases the resolution of the feature grid during training. In contrast, KiloNeRF (Reiser et al. 2021) uses numerous amount of tiny MLPs instead of one large MLP to dramatically reduce rendering time. SNeRG (Hedman et al. 2021) extracts view-dependent and color features from a trained NeRF, bakes them into a 3D texture atlas, and uses a relatively small MLP to synthesize novel views with the baked features. RT-NeRF (Li et al. 2022) performs fast rendering by back projecting the feature grid onto the render target image plane instead of using ray marching. Control-NeRF (Lazova et al. 2023) blends feature grids trained on different scenes to selectively render objects across the scenes.

A recent seminal work, Instant-NGP (Müller et al. 2022), maps multiresolution grids that encode a scene at various levels of abstraction onto a relatively small memory space using a hash function, allowing for the rapid learning of a plausible scene in seconds. In addition, TensorRF (Chen et al. 2022a) decomposes a deep feature grid into vectors and matrices, resulting in improved storage efficiency.

3 Method

3.1 Preliminary

Scene representation of neural radiance field NeRF (Mildenhall et al. 2020) uses MLP networks to learn the radiance field of arbitrary scenes. Once sufficiently optimized, NeRF can estimate both the volume density σ and RGB color \mathbf{c} of the continuous function that describes the radiance field. It is then able to reconstruct a photo-realistic view from an unseen pose using a differentiable volume rendering method.

Given a camera pose and pixel coordinates, NeRF generates a camera ray $\mathbf{r}(t) = \mathbf{o} + t\mathbf{d}$ that marches from $\mathbf{o} \in \mathbb{R}^3$ in direction $\mathbf{d} \in [-\pi, \pi]^2$ to the pixel and samples N points along the ray \mathbf{r} with a certain distribution. Each sampled point $\mathbf{x} \in \mathbb{R}^3$ is given as input to the MLP $F_\Phi : (\mathbf{x}, \mathbf{d}) \mapsto (\sigma, \mathbf{c})$. The MLP further infers the density $\sigma \in \mathbb{R}$ of the point \mathbf{x} and RGB color $\mathbf{c} \in \mathbb{R}^3$ corresponding to the ray direction \mathbf{d} . Taking into account the density σ_i and light transmittance T_i of each point \mathbf{x}_i , the final color $\hat{\mathbf{C}}(\mathbf{r})$ for the ray \mathbf{r} (i.e., the color of the pixel) is determined by a weighted sum of the colors of the N sampled points along

the ray \mathbf{r} , which can be formulated as:

$$\hat{\mathbf{C}}(\mathbf{r}) = \sum_{i=1}^N T_i (1 - \exp(-\sigma_i \delta_i)) \mathbf{c}_i, \quad (1)$$

$$T_i = \prod_{j<i} \exp(-\sigma_j \delta_j),$$

where δ_i is the distance between successive sampled points \mathbf{x}_i and \mathbf{x}_{i+1} , and i and j indicate the order of the sampled points.

Multiresolution hash encoding To enhance training efficiency without compromising reconstruction quality, prior NeRF methods (Sun, Sun, and Chen 2022a; Martel et al. 2021; Liu et al. 2020; Müller et al. 2022) opt to encode the radiance field using feature grids with small MLP network instead of training a large MLP on the entire scene.

Instant-NGP (Müller et al. 2022), as a representative work of this method, compresses multiple feature grids with different resolutions into dedicated hash tables for expressing smoothness and minimizing worthless grid points. Specifically, it owns two types of trainable parameters: encoding parameters Θ stored in the hash tables and weight parameters Φ for the NeRF Renderer. The encoding parameters are arranged into L hierarchical grid levels with distinct resolutions. Each grid point contains a feature vector with an F -dimensional size. Furthermore, every feature vector for a given grid resides in its respective l -th hash table, which has a maximum capacity of T . The resolution ratio b between successive grids is defined as follows:

$$b = (N_{max}/N_{min})^{1/(L-1)}, \quad (2)$$

where N_{max} and N_{min} are the maximum resolution and minimum resolution of grids, respectively. Hence, the resolution of l -th grid is given by:

$$N_l = \lfloor N_{min} \cdot b^{l-1} \rfloor \quad (3)$$

Given a sampled point \mathbf{x} and a viewing direction \mathbf{d} , Instant-NGP identifies the indices, $\mathbf{I}^{\mathcal{G}_l} = (i, j, k)$, of the eight voxel corners surrounding \mathbf{x} at each grids \mathcal{G}_l , resulting in the total of $8 \cdot L$ corner points. Then, the spatial hash $h(\cdot)$ (Teschner et al. 2003) is applied to each $\mathbf{I}^{\mathcal{G}_l}$ to retrieve the associated feature vector from the dedicated hash table θ_l :

$$h(\mathbf{I}^{\mathcal{G}_l}) = (i \cdot \pi_1 \oplus j \cdot \pi_2 \oplus k \cdot \pi_3) \bmod T, \quad (4)$$

where \oplus is bit-wise XOR operator, T is the hash table size, and π is a prime number (i.e., $\pi_1 = 1$, $\pi_2 = 2, 654, 435, 761$, and $\pi_3 = 805, 459, 861$). After that, the eight F -dimensional feature vectors are trilinearly interpolated resulting in $f_l \in \mathbb{R}^F$. Then, the L feature vectors are concatenated into $\mathbf{y} = [f_1; \dots; f_L]$, which serves as the input to the NeRF Renderer, with viewing direction \mathbf{d} . The NeRF Renderer is constructed by a density MLP m_d and a color MLP m_c which are parameterized by Φ_d and Φ_c (i.e., $\Phi = [\Phi_d; \Phi_c]$), respectively. The density σ and color \mathbf{c} estimation can be formulated like:

$$\begin{aligned} f_c &= m_d(\mathbf{y}; \Phi_d), \\ \sigma &= f_c[0], \\ \mathbf{c} &= m_c(f_c; \Phi_c), \end{aligned} \quad (5)$$

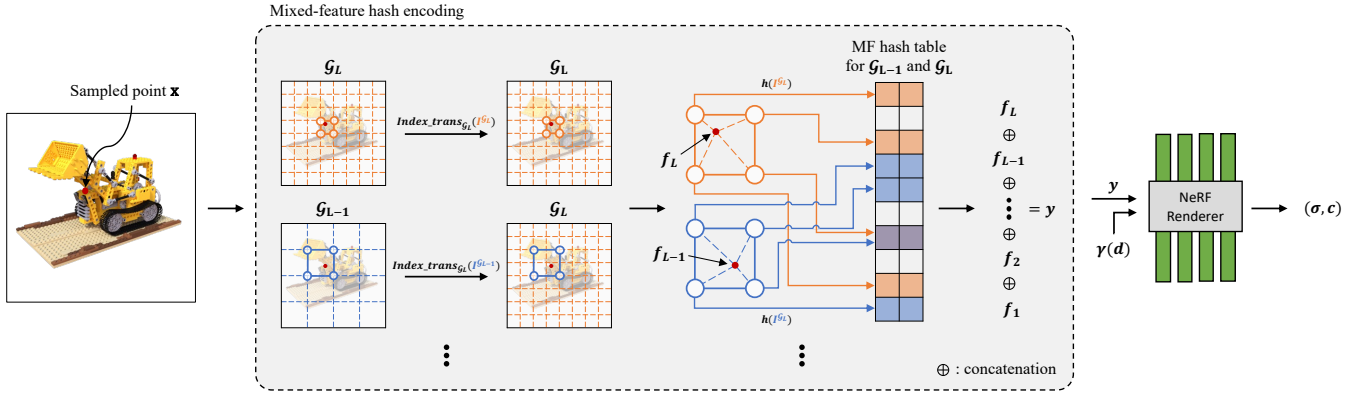


Figure 2: Overview of MF-NeRF in 2D representation. MF-NeRF employs mixed-feature hash encoding to share scene features across consecutive grids, allowing for mixing fine and coarse details. Indices from lower grids are remapped to the highest resolution grid sharing the same MF hash table, allowing grids to reference identical hash entries for congruent scene coordinates, as exemplified by the lower-right corners of the orange and blue voxels in the figure. After interpolating feature vectors of the corners, the NeRF Renderer processes these along with the positional embedded viewing direction $\gamma(d)$ to determine point \mathbf{x} 's density σ and color c . Our method could be simply extended to three dimensions as well.

where f_c represents the color features produced by the density MLP m_d .

Limitations of multiresolution hash encoding However, although the multiresolution hash encoding enables fast learning speed compared to conventional NeRF (Mildenhall et al. 2020), there still remain several limitations. First, it inefficiently uses multiple dense feature grids to represent vast empty spaces and occupied spaces that inherently exist in 3D space. Due to the uniformity of the object's interior, incident voxels within the object across different grids are prone to containing similar feature values. This also applies to the empty spaces, resulting in many voxels across the grids having similar feature values. Second, multiresolution hash encoding compresses features into multiple hash tables corresponding to feature grids of different resolutions via hash function, which means it has to manage the same number of feature grids with the feature resolution levels L . For example, coarse grid learns simple shapes and fine grid learns detailed shapes. Moreover, the features of each grid are saved in the different memory space, and the size of hash table T and feature resolution levels L crucially affect the learning capacity of Instant-NGP. This indicates that higher values of T and L are essential for effectively reconstructing high-quality scenes with more intricate details. However, this results in substantial encoding parameters, which is orders of magnitude larger than the weight parameters of the MLP. For instance, in a general setting of Instant-NGP with a hash table size T of 2^{19} and feature resolution levels L of 16, the resulting encoding parameter size is 12.6 M, which is $1,191\times$ larger than the weight parameter size (10k). The extensive memory usage due to large encoding parameters lead to a notable increase in computer cache miss ratio, consequently resulting in significantly longer training time, especially when T is larger than the size of computer cache (Müller et al. 2022). Likewise, this limitation could potentially restrict its practical implementation in real-world

scenarios, such as large-scale view synthesis or deployment on memory-limited edge devices.

3.2 Proposed MF-NeRF

In this section, we present MF-NeRF, a memory efficient NeRF framework with a novel **mixed-feature hash table** design to reduce memory usage and training time, all while preserving the quality of reconstruction as shown in Fig. 2. Unlike Instant-NGP which learns different levels of abstraction of the scene with dedicated grid size (namely, the number of grid with different sizes equal to the different resolution levels), the proposed mixed-feature hash encodes mix multiple grids into a shared hash table, enabling the learning of combined coarse and fine abstracted features. This design choice is based on the assumption that overlapping grids in the same radiance field likely exhibit analogous feature distributions. Thus, maintaining separate hash tables for each grid becomes redundant. Instead, we allow similar features from different grids to be stored in the same entry of a shared mixed-feature hash table.

Furthermore, to retrieve appropriate features from the MF hash table, we further design an **index transformation** method, which converts an index from a lower-level grid to a corresponding index in a higher-level grid linked via the same MF hash table. For each of the L grids, the feature vectors corresponding to the eight voxel corners are retrieved and trilinearly interpolated. Then, the L interpolated feature vectors are concatenated and fed into a series of MLPs to estimate the density and color values of the sample point. The detailed techniques will be introduced in the following sections.

Mixed-Feature Hash Encoding First of all, following the setting in the Instant-NGP (Müller et al. 2022), we construct L grids $\{\mathcal{G}_l\}_{l=1}^L$ with different resolution levels. The resolution ratio b between grid \mathcal{G}_l and \mathcal{G}_{l+1} aligns with definition as shown in Eq. 2.

To build mixed-feature hash table, we create $N \in [1, L]$ hash tables, each with a maximum size of $T \in [2^{14}, 2^{24}]$. In practice, the size of hash table size is given by $\min(T, N_{i,W}^3)$, where $i \in [1, N]$, and each entry holds an F -dimensional feature vector. The selection of hyperparameter N should be less than or equal to the number of grids L . For example, if N equals to L , the number of hash table is same as the multiresolution hash encoding; When $N = 1$, a single hash table is shared by all grids.

Furthermore, to mix multiple grids with different levels into one hash table, we develop an index transformation method to transform the current index space of these grids to the index space of the finest grid for each hash table with the corresponding grid groups (The detailed technique of index transformation will be introduced below). For example, given that $L = 8$ and $N = 2$, each 4 consecutive grids are encoded into one hash table. More specifically, when a sampled point \mathbf{x} is queried, the indices of the eight voxel corner points surrounding the point \mathbf{x} at each grids $\{\mathcal{G}_l\}_{l=1}^8$ will be first identified. Following that, the indices $\{\mathbf{I}^{\mathcal{G}_l}\}_{l=1}^4$ from the initial half of the grids are transformed to the corresponding indices $\mathbf{I}^{\mathcal{G}_4}$ of the 4th-level grid \mathcal{G}_4 , while the indices $\{\mathbf{I}^{\mathcal{G}_l}\}_{l=5}^8$ from the latter half are transformed to the corresponding indices $\mathbf{I}^{\mathcal{G}_8}$ of the 8th-level grid \mathcal{G}_8 .

Upon obtaining the transformed indices, they are hashed to find the entries in the defined hash table by using the spatial hash function as shown in Eq. 4. The resultant eight F -dimensional feature vectors undergo trilinear interpolation to produce $\{f_l\}_{l=1}^L$. These L feature vectors are concatenated as $\mathbf{y} = [f_1; \dots; f_L]$ and then fed into the NeRF Renderer (Eq. 5) alongside the viewing direction \mathbf{d} , yielding the density and color values of \mathbf{x} . By doing so, The mixed-feature (MF) hash table is built to consolidates partial grids within a single hash table. It allows the proposed MF-NeRF to learn mixed features of coarse and fine abstraction, leading to significantly feature size reduction.

Index Transformation Given that voxel size varies depending on grid resolution, grid points at identical positions in different grids might have distinct indices. For example, in Fig. 2, both the orange and blue voxels’ lower-right corners are located at the same position within the lego scene. However, their indices are (2, 2) in grid \mathcal{G}_{L-1} and (4, 4) in grid \mathcal{G}_L . When hashed, these indices map to different entries in the MF hash table despite representing the same spatial location. To address this, we employ an index transform function $Index.trans_{\mathcal{G}_j}(\cdot)$ to translate indices in arbitrary level grid \mathcal{G}_i into those in j -th level grid \mathcal{G}_j prior to hashing.

$$\begin{aligned} Index.trans_{\mathcal{G}_j}(\mathbf{I}^{\mathcal{G}_i}) &= [\mathbf{I}^{\mathcal{G}_i} \times N_j/N_i] \\ &= \mathbf{I}^{\mathcal{G}_j}, \end{aligned} \quad (6)$$

where $N_{\mathcal{G}_i}$ and $N_{\mathcal{G}_j}$ are resolutions of i -th and j -th grids calculated by Eq. 3. With this function, we obtain the indices in the finest grid, among those sharing the same MF hash table, for grid points of grids at any levels. Using consistent grid space indices when accessing the MF hash table ensures that multiple grids reference the same feature for a specific location.

Instant-NGP		MF-NeRF-1	
# Features (T)	PSNR	# Features (T)	PSNR
3,293,600 (2^{17})	32.69	2,097,152 (2^{20})	32.70
6,177,184 (2^{18})	32.76	4,194,304 (2^{21})	32.91
11,445,040 (2^{19})	32.91	8,388,608 (2^{22})	33.10
21,061,904 (2^{20})	32.97	16,777,216 (2^{23})	33.13

Table 1: MF-NeRF with one MF hash table (MF-NeRF-1) can learn a scene with smaller memory usage.

Training The proposed MF-NeRF is trained by using a set of posed images. Specifically, we jointly optimize both encoding and weight parameters by calculating the \mathcal{L}^2 loss between the rendered color $\hat{C}(\mathbf{r})$ and the ground truth color $C(\mathbf{r})$. The loss function is defined as:

$$Loss = \sum_{\mathbf{r} \in \mathcal{R}} \|\hat{C}(\mathbf{r}) - C(\mathbf{r})\|_2^2 \quad (7)$$

where \mathcal{R} is a batch of camera rays randomly sampled from all the pixels in the image set.

In summary, the whole training process can be illustrated as follows: given a sampled point \mathbf{x} and a viewing direction \mathbf{d} , MF-NeRF first obtains the voxel’s eight corner indices $\{\mathbf{I}^{\mathcal{G}_l}\}_{l=1}^L$ at each grids. Before hashing the eight $\mathbf{I}^{\mathcal{G}_l}$, these indices are transformed to the corresponding highest-resolution grid space by using the index transformation function. After this transformation, corresponding feature vectors are retrieved from the MF hash tables. The eight feature vectors corresponding to the voxel’s eight corner points are then trilinearly interpolated, resulting in one feature vector f_l for l -th level grid. Then, L interpolated feature vectors are concatenated (i.e., $\mathbf{y} = [f_1; \dots; f_L]$) and forwarded to the NeRF Renderer along with the viewing direction \mathbf{d} (Eq. 5).

4 Experiments

4.1 Experimental setup

Dataset We train MF-NeRF and the baselines on the widely-use Synthetic NeRF dataset (Mildenhall et al. 2020), which includes eight different synthetic scenes. Each scene contains 400 posed images: 100 for training, 100 for validation, and 200 for testing, all with a resolution of 800×800 . Additionally, we train on another popular MipNeRF360 dataset (Barron et al. 2022), which encompasses seven publicized, unbounded real scenes. Each scene consists of between 125 and 311 images. Since this dataset is not pre-split, we select every 8th image for testing. Image resolutions vary by scene, ranging from 3114×2075 to 4978×3300 .

Metric We employ three commonly used metrics to evaluate the performance: peak signal-to-noise ratio (PSNR), structural similarity index measure (SSIM) (Wang et al. 2004), and learned perceptual image patch similarity of VGG (LPIPS-VGG) (Zhang et al. 2018). These metrics quantify the similarity between the ground truth images and the reconstructed images.

Synthetic NeRF	# Features				PSNR				SSIM				LPIPS				Training Time (mins)			
	2^{20}	2^{21}	2^{22}	2^{23}	2^{20}	2^{21}	2^{22}	2^{23}	2^{20}	2^{21}	2^{22}	2^{23}	2^{20}	2^{21}	2^{22}	2^{23}	2^{20}	2^{21}	2^{22}	2^{23}
Instant-NGP	21.06 M	38.55 M	70.20 M	126.97 M	32.97	33.03	33.05	33.00	.9595	.9602	.9602	.9599	.0501	.0490	.0482	.0478	8.42	10.93	13.55	17.43
MF-NeRF-1	2.10 M	4.19 M	8.39 M	16.78 M	32.70	32.91	33.10	33.13	.9572	.9582	.9603	.9597	.0560	.0533	.0505	.0496	8.17	9.84	11.27	12.49
MF-NeRF-2	4.19 M	7.00 M	11.20 M	19.59 M	32.80	32.88	33.07	33.04	.9578	.9595	.9601	.9602	.0544	.0519	.0502	.0494	8.23	9.82	11.36	12.55
MF-NeRF-4	6.39 M	11.30 M	19.69 M	36.47 M	32.91	33.05	33.08	33.08	.9594	.9600	.9601	.9604	.0519	.0497	.0490	.0486	8.33	9.92	11.38	12.96
MF-NeRF-8	11.16 M	20.26 M	37.04 M	68.64 M	33.06	33.11	33.20	33.15	.9600	.9610	.9606	.9611	.0499	.0489	.0480	.0473	8.37	10.34	12.18	14.58

Table 2: Ablation study on different number of mixed-feature tables and table sizes. The trailing numbers of MF-NeRF- indicates the number of MF hash tables N .

Dataset	Method	# Features	PSNR	SSIM	LPIPS	Time
Synthetic NeRF	TensoRF	17.34 M	33.22	.9630	.0470	28.77
	DVGOv1	57.34 M	31.94	.9567	.0534	19.02
	DVGOv2	57.34 M	31.90	.9561	.0539	8.58
	Instant-NGP (2^{20})	21.06 M	32.97	.9595	.0501	8.42
	Instant-NGP (2^{22})	70.20 M	33.05	.9602	.0482	13.55
	MF-NeRF-8 (2^{20})	11.16 M	33.06	.9600	.0499	8.37
	MF-NeRF-8 (2^{22})	37.03 M	33.20	.9606	.0480	12.18
MipNeRF360	DVGOv2	57.34 M	25.70	.7043	.3654	24.41
	Instant-NGP (2^{20})	21.06 M	27.06	.7455	.3243	12.44
	Instant-NGP (2^{22})	70.20 M	27.36	.7699	.2939	22.81
	MF-NeRF-8 (2^{20})	11.16 M	27.11	.7400	.3342	11.78
	MF-NeRF-8 (2^{22})	37.03 M	27.38	.7641	.3016	20.31

Table 3: Quantitative comparison with SOTA works (the numbers in the parentheses of methods indicate the hash table size T)

Baselines: We consider Instant-NGP (Müller et al. 2022) as our baseline which uses a multiresolution hash table to encode scene features. Moreover, we also compare to other two SOTA methods: TensoRF (Chen et al. 2022a), DVGOv1 (Sun, Sun, and Chen 2022a), and DVGOv2 (Sun, Sun, and Chen 2022b).

Implementation details We adopt Adam (Kingma and Ba 2014) optimizer with an initial learning rate of $2 \cdot 10^{-2}$, which decreased to $2 \cdot 10^{-4}$ using cosine decay. The random seed is set to 1337. All the synthetic scenes are trained with the same hyperparameters, including a batch size of 16384, $N_{max} = 1024$, $N_{min} = 16$, $L = 16$, and $F = 2$. For the unbounded scenes, we train MF-NeRF with hyperparameters including a batch size of 4096, $N_{max} = 1024$, $N_{min} = 16$, $L = 16$, and $F = 2$. We use 0.25 times downsampled images for the unbounded scene training. We configure different scale factors for the unbounded scenes ($16\times$ for bicycle, bonsai, counter, and garden scenes; $4\times$ for kitchen and room scenes; $64\times$ for stump scene). We train 20k iterations for both synthetic and unbounded scenes on a single NVIDIA Quadro RTX 5000 GPU.

In our experiments, the density MLP is configured with a single hidden layer with 64 channels, while the color MLP consists of two hidden layers, each with 128 channels. Empirical testing led us to choose broader channels for the color MLP compared to Instant-NGP, maximizing the MLP’s performance. This optimized MLP offers improved capability in both mitigating hash collisions and translating color fea-

tures into more realistic colors. Unless otherwise specified, we set $N = 8$ for MF-NeRF as the default configuration.

4.2 Experimental Results

Scene compression First, we investigate how MF-NeRF can effectively compress a scene. To do so, we train MF-NeRF in the extreme case where there is only one single MF hash table (i.e., $N = 1$). To fair compare to Instant-NGP, we only adjust the hash table size, while keeping the other settings same. In Table 1, we show the results of training Instant-NGP and MF-NeRF-1 ($N = 1$, $W = 16$) on the Synthetic NeRF dataset (both methods have $L = 16$, $F = 2$, $N_{min} = 16$, $N_{max} = 1024$, batch = 16384, iters = 20k settings in common). It is intriguing to observe that MF-NeRF-1 achieves better performance than Instant-NGP with 20-36% fewer parameters. We believe this result suggests that Instant-NGP may suffers from unnecessary redundancy due to learn similar features among each grid.

Comparison with Instant-NGP While sharing a single hash table among all grids (i.e., MF-NeRF-1) can significantly reduce memory usage, it may also degrade learning performance due to excessively limited memory space. To determine the ideal value for N , we conduct experiments by doubling the number of MF hash tables from $N = 1$ up to $N = 8$. As shown in Table 2, we report the performance of MF-NeRF- N with different N settings of 1, 2, 4, and 8. Compared to Instant-NGP, we can see that MF-NeRF-8 achieved a parameter reduction of 47.01%/47.44%/47.24%/45.94%, and training time reductions of 3s/35s/82s/171s, with a 0.09/0.08/0.15/0.15 PSNR improvement at all four different T settings, respectively. In addition, it is interesting to see that as the hyperparameter T increased, MF-NeRF showed larger training time reductions compared to Instant-NGP, indicating that the larger parameters of Instant-NGP are a bottleneck that constrains its training time.

Benchmarking with SOTA methods We further compare the performance of MF-NeRF with other SOTA methods, including TensoRF (Chen et al. 2022a), DVGOv1 (Sun, Sun, and Chen 2022a), DVGOv2 (Sun, Sun, and Chen 2022b), and Instant-NGP (Müller et al. 2022) using the Synthetic NeRF and MipNeRF360 datasets. The comprehensive comparison results are reported in Table 3. For the Synthetic NeRF benchmark, although TensoRF shows overall high performance, it has the largest training time, with around

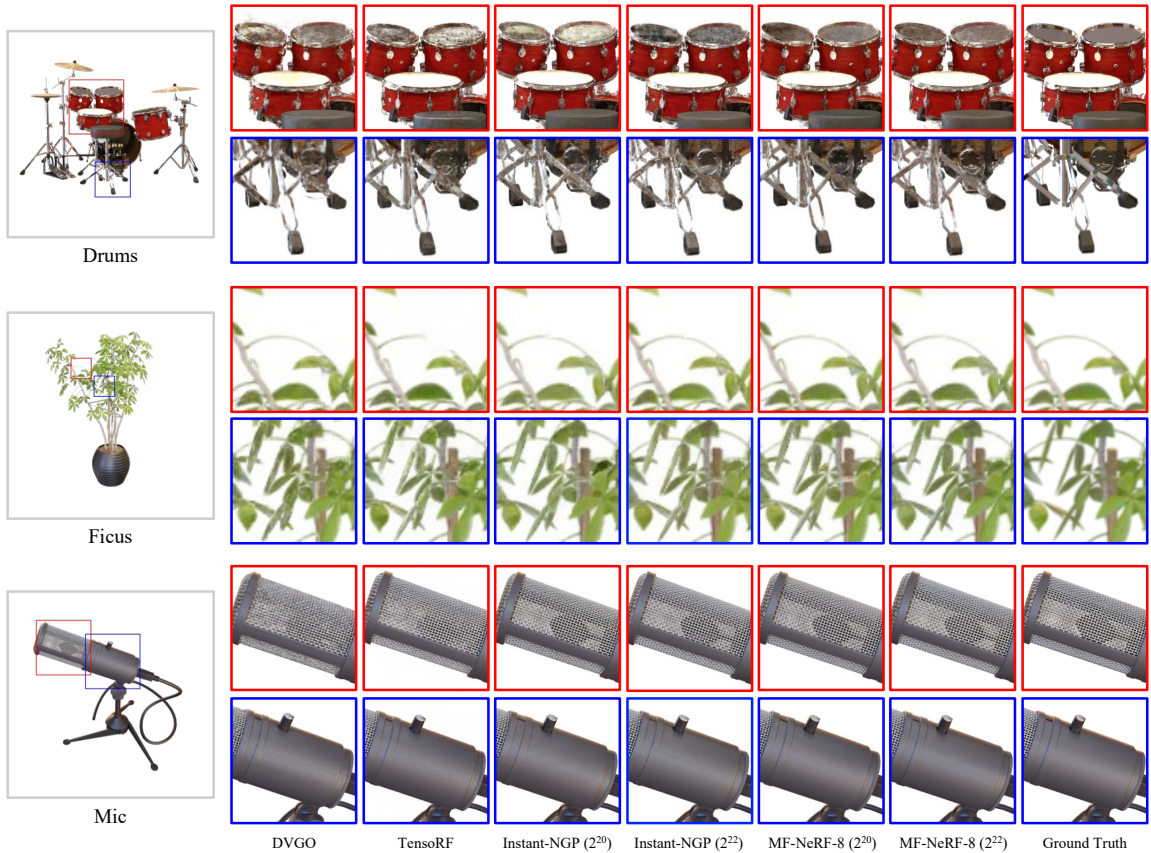


Figure 3: We present qualitative results on three scenes, comparing MF-NeRF-8 with other SOTA methods.

3.4 \times and 2.3 \times longer training time than our MF-NeRF-8 (2^{20}) and MF-NeRF-8 (2^{22}), respectively. However, the average PSNR difference is only 0.16 and 0.02, respectively. As can be seen, both MF-NeRF-8 (2^{20}) and MF-NeRF-8 (2^{22}) configurations learn the scenes faster and exhibit higher average PSNR and SSIM than DVGOv1. When considering the same T , MF-NeRF-8 consistently outperforms its Instant-NGP counterparts in terms of average PSNR and requires a shorter training time. Compared to DVGOv2, our MF-NeRF-8 (2^{20}) achieves better average PSNR and shorter training time on all synthetic scenes. Specifically, we achieve a 1.16 PSNR improvement and a slight 12s training time reduction on average. In addition, compared to TensoRF, our MF-NeRF-8 (2^{22}) achieves almost the same PSNR (i.e., 0.01 degradation) but significantly reduces the training time by up to 2.4 \times on average.

In the MipNeRF360 benchmark tests, our models MF-NeRF-8 (2^{20}) and MF-NeRF-8 (2^{22}) surpass DVGOv2, exhibiting average PSNR improvements of 1.41/1.68 respectively, alongside training time reductions of 51.74%/16.79%. Moreover, in comparisons with Instant-NGP of T counterpart, these models consistently showcase superior reconstruction, with PSNR enhancements of 0.05/0.02, and training time savings of 39s/150s, respectively.

4.3 Visualization

Fig. 3 shows a qualitative comparison between NeRF methods on the test images. When comparing the drum surface and legs, it can be observed that MF-NeRF depicts smoother and more accurate shading than Instant-NGP. We can also observe a similar phenomenon in the leaves, which Instant-NGP oddly depicts a dark green color. When considering volume reconstruction, MF-NeRF appears to not miss thin structures. MF-NeRF also recognizes the microphone sensor inside the thin mesh cover in the Mic scene and can depict slender branches without disconnection in the Ficus scene.

5 Conclusion

In this paper, we propose a novel framework for neural radiance field (NeRF) that employs a mixed-feature (MF) hash table to improve memory efficiency, and reduce training/rendering time, while maintaining reconstruction quality. By sharing the hash table, our method saves memory space for storing scene features and enhances the training speed by preventing multiple feature grids from redundantly learning the same feature. In the experiment, we observe that our proposed method achieves significant improvements in terms of training time reduction and rendering quality with smaller parameter size compared to the prior Instant-NGP method.

References

- Barron, J. T.; Mildenhall, B.; Tancik, M.; Hedman, P.; Martin-Brualla, R.; and Srinivasan, P. P. 2021. Mip-NeRF: A Multiscale Representation for Anti-Aliasing Neural Radiance Fields. In *2021 IEEE/CVF International Conference on Computer Vision (ICCV)*, 5835–5844. Los Alamitos, CA, USA: IEEE Computer Society.
- Barron, J. T.; Mildenhall, B.; Verbin, D.; Srinivasan, P. P.; and Hedman, P. 2022. Mip-NeRF 360: Unbounded Anti-Aliased Neural Radiance Fields. In *2022 IEEE/CVF Conference on Computer Vision and Pattern Recognition (CVPR)*, 5460–5469. New Orleans, LA, USA: IEEE. ISBN 978-1-6654-6946-3.
- Chen, A.; Xu, Z.; Geiger, A.; Yu, J.; and Su, H. 2022a. TensorRF: Tensorial Radiance Fields. In Avidan, S.; Brostow, G.; Cissé, M.; Farinella, G. M.; and Hassner, T., eds., *Computer Vision – ECCV 2022*, 333–350. Cham: Springer Nature Switzerland. ISBN 978-3-031-19824-3.
- Chen, M.; Zhang, J.; Xu, X.; Liu, L.; Cai, Y.; Feng, J.; and Yan, S. 2022b. Geometry-Guided Progressive NeRF for Generalizable and Efficient Neural Human Rendering. In Avidan, S.; Brostow, G.; Cissé, M.; Farinella, G. M.; and Hassner, T., eds., *Computer Vision – ECCV 2022*, 222–239. Cham: Springer Nature Switzerland. ISBN 978-3-031-20050-2.
- Chen, T.; Wang, P.; Fan, Z.; and Wang, Z. 2022c. AugNeRF: Training Stronger Neural Radiance Fields with Triple-Level Physically-Grounded Augmentations. In *2022 IEEE/CVF Conference on Computer Vision and Pattern Recognition (CVPR)*, 15170–15181. Los Alamitos, CA, USA: IEEE Computer Society.
- Chen, Z.; Funkhouser, T.; Hedman, P.; and Tagliasacchi, A. 2022d. MobileNeRF: Exploiting the Polygon Rasterization Pipeline for Efficient Neural Field Rendering on Mobile Architectures. 1–10. arXiv.
- Deng, K.; Liu, A.; Zhu, J.; and Ramanan, D. 2022. Depth-supervised NeRF: Fewer Views and Faster Training for Free. In *2022 IEEE/CVF Conference on Computer Vision and Pattern Recognition (CVPR)*, 12872–12881. Los Alamitos, CA, USA: IEEE Computer Society.
- Guo, M.; Li, C.; and Lee, G. H. 2022. Incremental Learning for Neural Radiance Field with Uncertainty-Filtered Knowledge Distillation. arXiv.
- Hedman, P.; Srinivasan, P. P.; Mildenhall, B.; Barron, J. T.; and Debevec, P. 2021. Baking Neural Radiance Fields for Real-Time View Synthesis. In *Proceedings of the IEEE/CVF International Conference on Computer Vision (ICCV)*, 5875–5884.
- Hong, Y.; Peng, B.; Xiao, H.; Liu, L.; and Zhang, J. 2022. HeadNeRF: A Realtime NeRF-based Parametric Head Model. In *2022 IEEE/CVF Conference on Computer Vision and Pattern Recognition (CVPR)*, 20342–20352. Los Alamitos, CA, USA: IEEE Computer Society.
- Hwang, I.; Kim, J.; and Kim, Y. M. 2023. Ev-NeRF: Event Based Neural Radiance Field. In *2023 IEEE/CVF Winter Conference on Applications of Computer Vision (WACV)*, 837–847. IEEE. ISBN 978-1-6654-9346-8.
- Johari, M.; Lepoittevin, Y.; and Fleuret, F. 2022. GeoNeRF: Generalizing NeRF with Geometry Priors. In *2022 IEEE/CVF Conference on Computer Vision and Pattern Recognition (CVPR)*, 18344–18347. Los Alamitos, CA, USA: IEEE Computer Society.
- Kingma, D. P.; and Ba, J. 2014. Adam: A Method for Stochastic Optimization. arXiv.
- Kurz, A.; Neff, T.; Lv, Z.; Zollhöfer, M.; and Steinberger, M. 2022. AdaNeRF: Adaptive Sampling for Real-Time Rendering of Neural Radiance Fields. In Avidan, S.; Brostow, G.; Cissé, M.; Farinella, G. M.; and Hassner, T., eds., *Computer Vision – ECCV 2022*, 254–270. Cham: Springer Nature Switzerland. ISBN 978-3-031-19790-1.
- Lazova, V.; Guzov, V.; Olszewski, K.; Tulyakov, S.; and Pons-Moll, G. 2023. Control-NeRF: Editable Feature Volumes for Scene Rendering and Manipulation. In *Proceedings of the IEEE/CVF Winter Conference on Applications of Computer Vision (WACV)*, 4340–4350.
- Lee, D.; and Lee, K. M. 2023. Dense Depth-Guided Generalizable NeRF. *IEEE Signal Processing Letters*, 30: 75–79.
- Li, C.; Li, S.; Zhao, Y.; Zhu, W.; and Lin, Y. 2022. RT-NeRF: Real-Time On-Device Neural Radiance Fields Towards Immersive AR/VR Rendering. In *Proceedings of the 41st IEEE/ACM International Conference on Computer-Aided Design, ICCAD '22*. New York, NY, USA: Association for Computing Machinery. ISBN 9781450392174.
- Lin, C.; Ma, W.; Torralba, A.; and Lucey, S. 2021. BARF: Bundle-Adjusting Neural Radiance Fields. In *2021 IEEE/CVF International Conference on Computer Vision (ICCV)*, 5721–5731. Los Alamitos, CA, USA: IEEE Computer Society.
- Liu, L.; Gu, J.; Zaw Lin, K.; Chua, T.-S.; and Theobalt, C. 2020. Neural Sparse Voxel Fields. In Larochelle, H.; Ranzato, M.; Hadsell, R.; Balcan, M. F.; and Lin, H., eds., *Advances in Neural Information Processing Systems*, volume 33, 15651–15663. Curran Associates, Inc.
- Ma, L.; Li, X.; Liao, J.; Zhang, Q.; Wang, X.; Wang, J.; and Sander, P. V. 2022. Deblur-NeRF: Neural Radiance Fields from Blurry Images. In *2022 IEEE/CVF Conference on Computer Vision and Pattern Recognition (CVPR)*, 12851–12860. Los Alamitos, CA, USA: IEEE Computer Society.
- Martel, J. N. P.; Lindell, D. B.; Lin, C. Z.; Chan, E. R.; Monteiro, M.; and Wetzstein, G. 2021. Acorn: Adaptive Coordinate Networks for Neural Scene Representation. *ACM Trans. Graph.*, 40(4).
- Martin-Brualla, R.; Radwan, N.; Sajjadi, M. M.; Barron, J. T.; Dosovitskiy, A.; and Duckworth, D. 2021. NeRF in the Wild: Neural Radiance Fields for Unconstrained Photo Collections. In *2021 IEEE/CVF Conference on Computer Vision and Pattern Recognition (CVPR)*, 7206–7215. Los Alamitos, CA, USA: IEEE Computer Society.
- Mildenhall, B.; Hedman, P.; Martin-Brualla, R.; Srinivasan, P. P.; and Barron, J. T. 2022. NeRF in the Dark: High Dynamic Range View Synthesis from Noisy Raw Images. In *2022 IEEE/CVF Conference on Computer Vision and Pattern Recognition (CVPR)*, 16169–16178. Los Alamitos, CA, USA: IEEE Computer Society.

- Mildenhall, B.; Srinivasan, P. P.; Tancik, M.; Barron, J. T.; Ramamoorthi, R.; and Ng, R. 2020. NeRF: Representing Scenes as Neural Radiance Fields for View Synthesis. In Vedaldi, A.; Bischof, H.; Brox, T.; and Frahm, J.-M., eds., *Computer Vision – ECCV 2020*, 405–421. Cham: Springer International Publishing. ISBN 978-3-030-58452-8.
- Müller, T.; Evans, A.; Schied, C.; and Keller, A. 2022. Instant Neural Graphics Primitives with a Multiresolution Hash Encoding. *ACM Trans. Graph.*, 41(4): 102:1–102:15.
- Niemeyer, M.; Mescheder, L.; Oechsle, M.; and Geiger, A. 2020. Differentiable Volumetric Rendering: Learning Implicit 3D Representations Without 3D Supervision. In *2020 IEEE/CVF Conference on Computer Vision and Pattern Recognition (CVPR)*, 3501–3512. Los Alamitos, CA, USA: IEEE Computer Society.
- Orsingher, M.; Zani, P.; Medici, P.; and Bertozzi, M. 2022. Learning Neural Radiance Fields from Multi-View Geometry. arXiv.
- Park, J.; Florence, P.; Straub, J.; Newcombe, R.; and Lovegrove, S. 2019. DeepSDF: Learning Continuous Signed Distance Functions for Shape Representation. In *2019 IEEE/CVF Conference on Computer Vision and Pattern Recognition (CVPR)*, 165–174. Los Alamitos, CA, USA: IEEE Computer Society.
- Pearl, N.; Treibitz, T.; and Korman, S. 2022. NAN: Noise-Aware NeRFs for Burst-Denoising. In *2022 IEEE/CVF Conference on Computer Vision and Pattern Recognition (CVPR)*, 12662–12671. Los Alamitos, CA, USA: IEEE Computer Society.
- Peng, C.; and Chellappa, R. 2022. PDRF: Progressively Deblurring Radiance Field for Fast and Robust Scene Reconstruction from Blurry Images. arXiv.
- Reiser, C.; Peng, S.; Liao, Y.; and Geiger, A. 2021. KiloNeRF: Speeding up Neural Radiance Fields with Thousands of Tiny MLPs. In *2021 IEEE/CVF International Conference on Computer Vision (ICCV)*, 14315–14325. Los Alamitos, CA, USA: IEEE Computer Society.
- Schonberger, J. L.; and Frahm, J. 2016. Structure-from-Motion Revisited. In *2016 IEEE Conference on Computer Vision and Pattern Recognition (CVPR)*, 4104–4113. Los Alamitos, CA, USA: IEEE Computer Society.
- Schönberger, J. L.; Zheng, E.; Frahm, J.-M.; and Pollefeys, M. 2016. Pixelwise View Selection for Unstructured Multi-View Stereo. In Leibe, B.; Matas, J.; Sebe, N.; and Welling, M., eds., *Computer Vision – ECCV 2016*, 501–518. Cham: Springer International Publishing. ISBN 978-3-319-46487-9.
- Schwarz, K.; Liao, Y.; Niemeyer, M.; and Geiger, A. 2020. GRAF: Generative Radiance Fields for 3D-Aware Image Synthesis. In *Proceedings of the 34th International Conference on Neural Information Processing Systems, NIPS’20, 20154–20166*. Red Hook, NY, USA: Curran Associates Inc. ISBN 9781713829546.
- Suhail, M.; Esteves, C.; Sigal, L.; and Makadia, A. 2022. Light Field Neural Rendering. In *2022 IEEE/CVF Conference on Computer Vision and Pattern Recognition (CVPR)*, 8259–8269. Los Alamitos, CA, USA: IEEE Computer Society.
- Sun, C.; Sun, M.; and Chen, H. 2022a. Direct Voxel Grid Optimization: Super-fast Convergence for Radiance Fields Reconstruction. In *2022 IEEE/CVF Conference on Computer Vision and Pattern Recognition (CVPR)*, 5449–5459. Los Alamitos, CA, USA: IEEE Computer Society.
- Sun, C.; Sun, M.; and Chen, H.-T. 2022b. Improved Direct Voxel Grid Optimization for Radiance Fields Reconstruction. arXiv.
- Takikawa, T.; Litalien, J.; Yin, K.; Kreis, K.; Loop, C.; Nowrouzezahrai, D.; Jacobson, A.; McGuire, M.; and Fidler, S. 2021. Neural Geometric Level of Detail: Real-time Rendering with Implicit 3D Shapes. In *2021 IEEE/CVF Conference on Computer Vision and Pattern Recognition (CVPR)*, 11353–11362. Los Alamitos, CA, USA: IEEE Computer Society.
- Tancik, M.; Casser, V.; Yan, X.; Pradhan, S.; Mildenhall, B. P.; Srinivasan, P.; Barron, J. T.; and Kretzschmar, H. 2022. Block-NeRF: Scalable Large Scene Neural View Synthesis. In *2022 IEEE/CVF Conference on Computer Vision and Pattern Recognition (CVPR)*, 8238–8248. Los Alamitos, CA, USA: IEEE Computer Society.
- Teschner, M.; Heidelberger, B.; Müller, M.; Pomeranets, D.; and Gross, M. 2003. Optimized Spatial Hashing for Collision Detection of Deformable Objects. In *VMV03: Proceedings of the Vision, Modeling, Visualization*, volume 3, 47–54. Munich.
- Turki, H.; Ramanan, D.; and Satyanarayanan, M. 2022. Mega-NeRF: Scalable Construction of Large-Scale NeRFs for Virtual Fly-Throughs. In *2022 IEEE/CVF Conference on Computer Vision and Pattern Recognition (CVPR)*, 12912–12921. Los Alamitos, CA, USA: IEEE Computer Society.
- Vaswani, A.; Shazeer, N.; Parmar, N.; Uszkoreit, J.; Jones, L.; Gomez, A. N.; Kaiser, .; and Polosukhin, I. 2017. Attention is All you Need. In Guyon, I.; Luxburg, U. V.; Bengio, S.; Wallach, H.; Fergus, R.; Vishwanathan, S.; and Garnett, R., eds., *Advances in Neural Information Processing Systems*, volume 30 of *NIPS’17*, 60006010. Curran Associates, Inc.
- Wang, D.; Cui, X.; Salcudean, S.; and Wang, Z. J. 2022. Generalizable Neural Radiance Fields for Novel View Synthesis with Transformer. arXiv.
- Wang, Q.; Wang, Z.; Genova, K.; Srinivasan, P.; Zhou, H.; Barron, J. T.; Martin-Brualla, R.; Snavely, N.; and Funkhouser, T. 2021. IBRNet: Learning Multi-View Image-Based Rendering. In *2021 IEEE/CVF Conference on Computer Vision and Pattern Recognition (CVPR)*, 4688–4697. Los Alamitos, CA, USA: IEEE Computer Society.
- Wang, Z.; Bovik, A. C.; Sheikh, H. R.; and Simoncelli, E. P. 2004. Image quality assessment: from error visibility to structural similarity. *IEEE Transactions on Image Processing*, 13(4): 600–612.
- Wei, Y.; Liu, S.; Rao, Y.; Zhao, W.; Lu, J.; and Zhou, J. 2021. NerfingMVS: Guided Optimization of Neural Radiance Fields for Indoor Multi-view Stereo. In *2021*

IEEE/CVF International Conference on Computer Vision (ICCV), 5590–5599. Los Alamitos, CA, USA: IEEE Computer Society.

Yen-Chen, L.; Florence, P.; Barron, J. T.; Rodriguez, A.; Isola, P.; and Lin, T.-Y. 2021. iNeRF: Inverting Neural Radiance Fields for Pose Estimation. In *2021 IEEE/RSJ International Conference on Intelligent Robots and Systems (IROS)*, 1323–1330.

Yu, A.; Li, R.; Tancik, M.; Li, H.; Ng, R.; and Kanazawa, A. 2021. PlenOctrees for Real-time Rendering of Neural Radiance Fields. In *2021 IEEE/CVF International Conference on Computer Vision (ICCV)*, 5732–5741. IEEE Computer Society.

Zhang, R.; Isola, P.; Efros, A. A.; Shechtman, E.; and Wang, O. 2018. The Unreasonable Effectiveness of Deep Features as a Perceptual Metric. In *2018 IEEE/CVF Conference on Computer Vision and Pattern Recognition (CVPR)*, 586–595. Los Alamitos, CA, USA: IEEE Computer Society.

Appendix A. Experiment detail

We present detailed experimental results for each individual scene. Our experiments is conducted on the Synthetic NeRF (?) and MipNeRF360 (?) datasets. As mentioned in the main text, we maintain consistent hyperparameters across the datasets with the exceptions of the image downsampling ratio, batch size, and scene scaling factor. We will elaborate on these scene-specific hyperparameter settings in a subsequent section. All other parameters are held constant, as summarized in Table 1, which are used for MF-NeRF and Instant-NGP (?).

Hyper-parameter	Description	Value
F	Number of features per hash table entry	2
L	Number of feature grids	16
N_{\min}	Coarsest resolution of feature grid	16
N_{\max}	Finest resolution of feature grids	1024
lr	Learning rate	$2 \cdot 10^{-2}$
decay	Learning rate decay factor	$1 \cdot 10^{-2}$
iters	Number of algorithm steps	20k
scale	Scene scaling factor	1
seed	Random seed	1337

Table 1: Common hyperparameters for MF-NeRF and Instant-NGP over the three datasets.

For DVGOv1 (?), DVGOv2 (?), and TensorRF (?), we use their default hyperparameter settings. We built our method directly on the CUDA code of Instant-NGP. However, for easy benchmarking of datasets not supported by Instant-NGP, we utilized the python implementation of Instant-NGP named ‘ngp-pl’ available at <https://github.com/kwea123/ngp-pl>.

Synthetic NeRF dataset comprises eight scenes: Chair, Drums, Ficus, Hotdog, Lego, Materials, Mic, and Ship. Each scene provides 400 images with a resolution of 800×800 . These images are divided as follows: 200 for training, 100 for evaluating, and 100 for testing. As the evaluation dataset is generally not utilized, we have omitted it, focusing solely on the training and testing datasets. We employed a consistent set of hyperparameters across all eight scenes for the MF-NeRF and Instant-NGP models: an image downsampling ratio of 1, a batch size of 16384, and a scene scaling factor of 1. The results are presented in Table 3 and Fig. 1.

MipNeRF360 dataset comprises seven scenes having backgrounds. These scenes are: Bicycle (194 images), Bonsai (292 images), Counter (240 images), Garden (185 images), Kitchen (279 images), Room (311 images), and Stump (125 images). We detail the properties and scale settings of these scenes in Table 2. For MF-NeRF and Instant-NGP model training, we employed a 1/4 downsampling ratio and used batches of 4096 rays. The results can be found in Table 4 and Fig. 2.

Scene	Original resolution	Train/Test split images	Scale
Bicycle	4946×3286	169/25	16
Bonsai	3118×2078	255/37	16
Counter	3115×2076	210/30	16
Garden	5187×3361	161/24	16
Kitchen	3115×2078	244/35	4
Room	3114×2075	272/39	4
Stump	4978×3300	109/16	64

Table 2: Scene by scene properties and scale hyperparameter setting.

Metrics	Methods	Chair	Drums	Ficus	Hotdog	Lego	Materials	Mic	Ship	Avg.
PSNR	TensoRF	35.77	25.93	34.12	37.58	36.59	30.11	34.95	30.71	33.22
	DVGOv1	34.08	25.46	32.78	36.70	34.56	29.58	33.20	29.13	31.94
	DVGOv2	34.06	25.40	32.56	36.75	34.67	29.58	33.18	29.02	31.90
	Instant-NGP (2^{20})	35.47	25.69	33.84	37.47	35.88	29.49	35.63	30.32	32.97
	Instant-NGP (2^{22})	35.49	25.79	34.03	37.41	36.00	29.53	35.88	30.30	33.05
	MF-NeRF-8 (2^{20})	35.55	25.89	34.21	37.41	35.98	29.54	35.4	30.49	33.06
	MF-NeRF-8 (2^{22})	35.74	25.95	34.03	37.46	36.27	29.58	35.86	30.71	33.20
SSIM	TensoRF	.9845	.9363	.9827	.9828	.9835	.9523	.9886	.8938	.9630
	DVGOv1	.9766	.9304	.9785	.9799	.9756	.9509	.9828	.8788	.9567
	DVGOv2	.9758	.9292	.9774	.9801	.9763	.9503	.9827	.8771	.9561
	Instant-NGP (2^{20})	.9800	.9313	.9813	.9804	.9798	.9450	.9888	.8891	.9595
	Instant-NGP (2^{22})	.9819	.9326	.9821	.9805	.9807	.9453	.9894	.8891	.9602
	MF-NeRF-8 (2^{20})	.9814	.9320	.9826	.9807	.9800	.9454	.9878	.8901	.9600
	MF-NeRF-8 (2^{22})	.9810	.9338	.9818	.9813	.9813	.9465	.9895	.8894	.9606
LPIPS	TensoRF	.0219	.0719	.0220	.0304	.0178	.0584	.0146	.1386	.0470
	DVGOv1	.0269	.0769	.0239	.0340	.0282	.0578	.0173	.1619	.0534
	DVGOv2	.0276	.0797	.0254	.0336	.0269	.0586	.0177	.1615	.0539
	Instant-NGP (2^{20})	.0223	.0781	.0262	.0360	.0211	.0677	.0173	.1318	.0501
	Instant-NGP (2^{22})	.0212	.0765	.0255	.0354	.0198	.0659	.0162	.1253	.0482
	MF-NeRF-8 (2^{20})	.0216	.0772	.0238	.0346	.0215	.0687	.0189	.1333	.0499
	MF-NeRF-8 (2^{22})	.0210	.0754	.0255	.0330	.0193	.0653	.0158	.1284	.0480
Training Time	TensoRF	23.41	24.15	29.18	29.40	26.91	40.70	19.94	36.48	28.77
	DVGOv1	17.27	16.95	18.35	21.43	18.23	21.32	15.27	23.37	19.02
	DVGOv2	7.98	7.90	8.03	9.05	8.55	9.23	6.85	11.03	8.58
	Instant-NGP (2^{20})	7.331	6.925	5.585	9.754	8.56	7.93	5.59	15.7	8.42
	Instant-NGP (2^{22})	11.88	11.13	8.76	15.79	13.82	12.59	8.85	25.61	13.55
	MF-NeRF-8 (2^{20})	7.29	6.74	5.06	9.77	8.39	8.04	5.17	16.47	8.37
	MF-NeRF-8 (2^{22})	10.47	9.72	7.12	14.00	12.36	11.34	7.16	25.27	12.18

Table 3: Scene by scene results on a synthetic dataset (Synthetic NeRF).



Figure 1: Qualitative result on Synthetic NeRF dataset.

Metrics	Methods	Bicycle	Bonsai	Counter	Garden	Kitchen	Room	Stump	Avg.
PSNR	DVGOv2	22.09	28.27	26.13	24.38	26.49	28.97	23.57	25.70
	Instant-NGP (2^{20})	23.21	30.80	26.88	24.95	30.27	29.94	23.39	27.06
	Instant-NGP (2^{22})	23.39	31.29	27.16	25.44	30.52	30.08	23.62	27.36
	MF-NeRF-8 (2^{20})	23.64	30.87	26.95	24.7	30.18	29.96	23.48	27.11
	MF-NeRF-8 (2^{22})	23.50	31.46	27.4	25.29	30.66	30.25	23.12	27.38
SSIM	DVGOv2	.4798	.8444	.7861	.6297	.7373	.8714	.5816	.7043
	Instant-NGP (2^{20})	.5263	.9144	.8036	.6489	.8831	.8947	.5474	.7455
	Instant-NGP (2^{22})	.5543	.9246	.8250	.6998	.8983	.9041	.5833	.7699
	MF-NeRF-8 (2^{20})	.5308	.9126	.7979	.6238	.8755	.8940	.5451	.7400
	MF-NeRF-8 (2^{22})	.5508	.9256	.8278	.6833	.8993	.9046	.5573	.7641
LPIPS	DVGOv2	.5107	.2817	.3191	.3765	.3057	.3054	.4586	.3654
	Instant-NGP (2^{20})	.5122	.1971	.3020	.3403	.1754	.2578	.4855	.3243
	Instant-NGP (2^{22})	.4814	.1705	.2715	.2984	.1536	.2312	.4510	.2939
	MF-NeRF-8 (2^{20})	.5091	.2058	.3142	.3621	.1846	.2675	.4960	.3342
	MF-NeRF-8 (2^{22})	.4884	.1721	.2707	.3145	.1543	.2374	.4736	.3016
Training Time	DVGOv2	27.10	23.68	24.55	24.18	21.92	23.42	26.03	24.41
	Instant-NGP (2^{20})	11.68	11.35	13.23	12.86	10.22	8.50	19.26	12.44
	Instant-NGP (2^{22})	22.62	22.40	22.27	24.70	18.63	16.13	32.91	22.81
	MF-NeRF-8 (2^{20})	10.02	12.13	12.48	13.62	9.85	8.74	15.61	11.78
	MF-NeRF-8 (2^{22})	19.16	20.49	20.43	21.90	16.82	15.48	27.87	20.31

Table 4: Scene by scene results on a unbounded dataset (MipNeRF360).

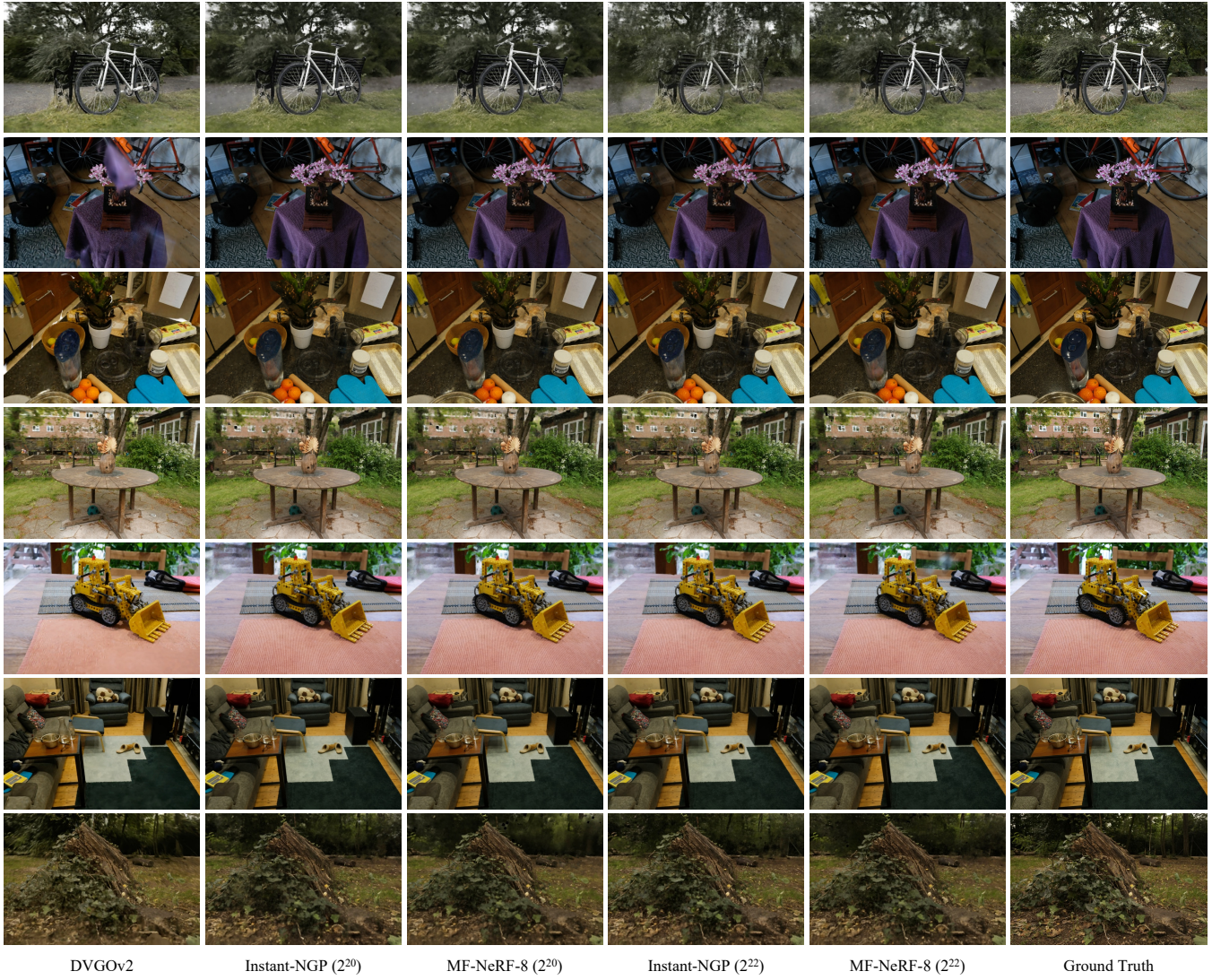


Figure 2: Qualitative result on the MipNeRF360 dataset.